

# Generating and Growing the Fractal City

Mandelbrot has attracted the attention of scientists on the ubiquity of fractal shapes among natural objects. This was an important and fruitful contribution. What is still missing in general is an understanding of how fractal shapes arise. (Ruelle, 1991, p. 178.)

## 8.1 Simulating Growth

Fractals have caught our imagination because the geometric patterns that they weave seem superficially simple, but on further scrutiny reveal infinite complexity through their self-similarity. Our fascination with them thus revolves around the mystery of explaining the myriad of processes which give rise to such patterns, and as David Ruelle (1991) suggests above, our concern for their geometry is only just giving way to a serious study of the dynamics of this pattern creation. Most of our knowledge of fractals so far is based upon methods for describing their geometry in the manner we began to illustrate in Chapter 2, and as yet, our knowledge of the way fractal structures emerge and evolve – their dynamics – is rudimentary. In this book, our use of fractal geometry in modeling city systems, and the limitations and potential which it displays is little different from many other domains in which this geometry is being developed. However, the DLA model which we developed in Chapter 7 and its generalization which we will seek in this chapter probably still represents the most promising approach to fractal dynamics (Orbach, 1986).

The ideal approach to a fractal dynamics of cities would be based on detailed histories of the development process in which the location of each behaving unit and its characteristics are recorded in time and space. As we noted in the last chapter, such histories are rarely available, certainly not from secondary data. The best we can hope for without engaging in massive primary survey, are time-series assembled from isolated observations of the system development at cross-sections in time, ideally on a regular time scale but unlikely at intervals finer than five years. In short, all we have are snapshots of development through time from which we can only infer the system's underlying dynamic. The pictures of London and Berlin, for example in Figures 7.3 and 7.4, provide the most detailed dynamics we have

available in the empirical work reported in this book. Thus for the most part, we are forced back to grounding and validating our models of fractal processes in terms of the ultimate development of the system at a single point in time; this was how we compared Taunton against the DLA model and how we will compare the town of Cardiff with the dielectric breakdown model (DBM) which is the subject of this chapter.

Yet despite these limitations posed by data, we can turn our attention away from comparisons of ultimate outcomes from static models of urban development patterns, to more detailed simulations of the growth process. As we illustrated in Chapter 7, the DLA model provides a rich dynamics with many similarities to the way urban development takes place. Indeed, one of the themes implicit in our notion of the fractal city is that the models we are proposing are not necessarily immediately applicable to real cities *per se* but enable us to work toward a general theory of cities. As such, fractal geometry changes the way we think about and observe the development of cities. There are, of course, many ways in which we might fine-tune our fractal models to real examples and we will demonstrate some of these in this chapter. But unlike more mainstream simulation models useful in urban analysis and planning, our approach separates models from their applications far more strictly than the norm. The example which we use here – based on Cardiff – simply provides the geometric container or the physical space within which we are able to grow a fractal cluster using DLA or DBM. In this sense then, our applications will emphasize the way in which the real geometry of the system interacts with a standard fractal dynamics to provide a simulation which best mirrors the reality.

In the more mainstream modeling of city systems, there is much less emphasis on the geometry of the system and how this molds and constrains development, and thus more concern for fine-tuning the dynamics of the simulation to the particular reality. Of course it is possible to fine-tune fractal models in this way, and in related work, we have explored how this might be done by altering the way particles aggregate and diffuse in DLA (Fotheringham, Batty and Longley, 1989). But here our focus will be upon showing how realistic urban systems can be simulated by growing ‘pure’ fractal clusters, but within geometrically ‘impure’ physical systems where the constraints and local conditions of the geometry are specified exogenously. It is these exogenous factors which we would not expect a fractal model to be able to replicate. An example is in order. If a fractal cluster growing in an unrestricted space according to a DLA interpretation of urban dynamics were to meet some physical barrier such as a mountain range which would distort its growth, ways of breaching the barrier might be necessary. Such breaches would clearly have to be input from outside the model. Although the model might be able to simulate the build-up of pressure against such a barrier which in turn might imply a need for some decision to breach it, the ultimate decision would have to be made outside the model and input as data to the process. It might be possible to link the model to another submodel of such decision-making, for example in the case of the mountain, a model which would predict what roads, bridges, tunnels and so on might be built. But these factors are outside the remit of the models we are working with here, and thus effective simulation of urban systems using fractal dynamics can only come through a judicious

manipulation of fractal growth processes with the geometry of the real system under study.

The model we developed in the last chapter was able to generate fractal structures whose self-similarity was dendritic or tree-like (Feder, 1988). These structures are far-from-equilibrium and, like cities, display a high degree of order. Such systems are the result of irreversible growth which keeps the structure intact; growth does not turn to decline, and thus the dynamics of development remain simple. As we have noted, such irreversibility is not the case for urban development, but the existence of models which link growth to form in such a simple way, yet generate richly ordered structures, is attractive as an analogy for city growth. Such parsimony provides a useful benchmark or baseline model which accounts for a substantial amount of all development, whilst enabling us to relax its assumptions slowly, one by one, in adding more realistic detail.

The model we will explore here generates a variety of urban forms of the dendritic type whose actual structures range from the linear to the concentric. Their units of development or 'particles' as we will continue to refer to them (Jullien and Botet, 1987), locate around a core or seed site such as the CBD. This DLA model which generates ramified dendritic structures around the seed site, is based on a simple process of diffusion which is limited by contact with the growing cluster of particles. It mirrors how a city might grow around a CBD with particles diffusing from a distant source which controls the amount of growth the city could attract, eventually reaching the growing city and sticking irreversibly once contact had been made. Its fractal dynamic is based on diffusion by random walk. Walkers are released one by one, at a far distance from the cluster, and then wander randomly on a lattice, one lattice step at a time, eventually walking away from the system and being 'killed' or towards the seed site, thus adding to the growing cluster. The emergence of a tree-like structure is a result of the fact that the particular places where the particles stick to the cluster are randomly formed. As branches begin to grow, these reinforce the structure. It is clear that the dendrite which is formed is the result of noise in the system, for, if the process of working towards the cluster was not random, an amorphous mass with little order would form. Thus it is noise or randomness which causes structure of the most articulate and ordered kind, a surprising conclusion perhaps, but one which is also emerging in the study of evolution and adaptation (Allen, 1982; Levy, 1992; Lewin, 1992; Waldrop, 1992).

The structure generated is fractal in the following sense: the mass of the dendrite created is less than the mass of the space that it occupies. Imagine a circular space in which the cluster is grown around the center of the circle. The dendrite occupies 'more' space than the line across the circle (its diameter say) but 'less' space than the entire circle itself. The line has dimension  $E = 1$ , the circle  $E = 2$ , and it is intuitively attractive to think of the dendrite as having a fractal dimension  $D$  between 1 and 2. In this chapter we will reformulate the model as a diffusion process in a potential field, using the logic of the dielectric breakdown model (DBM). This is done to show how the model is able to generate a continuum of forms by systematic distortion of the potential field. The fractal case is the 'pure' case where there is no distortion of the field and where we refer to this as the 'baseline'

model. We will introduce a parameter to control the distortion and show how forms can be generated which are reminiscent of ideal linear cities with  $D$  (and  $E$ ) = 1 to radial–concentric cities with  $D$  (and  $E$ ) = 2, the forms in-between embodying a continuum of city shapes with fractional dimension. Moreover, it is absolutely essential to formulate and solve this DLA model mathematically if an efficient means for generating these forms is to be developed.

We will first explore the relationship between DLA and DBM (which we will call the continuum model) and then show how we can solve the model. We will show how the fractal dimension can be measured with respect to the distributions of particles and their densities, introducing conventional but slow, then approximate but fast methods of estimation. A typical solution of the model based on a  $300 \times 300$  lattice is presented in terms of its spatial properties and its fractal dimensions are estimated using the procedures outlined in Chapter 7. As the model is based on random site selection, it is necessary to see how its forms vary with respect to this randomness, and the stability of its form and dimension is then evaluated over several runs of the model, showing how robust the procedures are. A circular space has been assumed, but in comparison with real city systems, such circularity is unrealistic. Therefore the effect of ‘taking out’ larger and larger sectors of the circle, and the resultant model forms, are presented, demonstrating how both dimension and form are affected. We are then in a position to see how a variety of such forms can be generated by varying the control parameter on the potential field of the model, thus illustrating how a continuum can be simulated. Finally, we will show how the model might be used to mimic reality using data pertaining to urban development in the medium-sized town of Cardiff.

## 8.2 Diffusion-Limited Aggregation and Dielectric Breakdown

In diffusion-limited aggregation, a source of diffusion is assumed at a distance far enough from the seed to have no effect upon the isotropy of the plane around the growing cluster. The source is modeled on a distant circle where particles are released one at a time, to begin a random walk on a lattice, usually square with unit spacing, progressing in any of the four adjacent directions on the grid. If the walker goes outside another circle defining the ‘sphere of influence’ of the cluster, its walk is terminated and another walker is released from the source. If the walker remains on the lattice, it will eventually touch a lattice point adjacent to the cluster where it sticks irreversibly. Another walker is then released. Because the sticking point is essentially random, initial perturbations from a compact cluster are exaggerated and branches form. Walkers are more likely to reach the tips of these branches than the crevasses in between, the tips effectively screening the crevasses from potential growth. A useful explanation of this process is given by Sander (1987).

As we illustrated in Chapter 7, the emerging dendritic cluster does not fill the space, but it is not as sparse as a line of particles running across the space. In short, the number of particles,  $N(R)$ , at a distance  $R$  from the seed scales according to a fractional power law,  $N(R) \approx R^D$ , where  $D$  is the fractal dimension and  $1 < D < 2$ . Witten and Sander (1983) argue that  $D = 1.70 \pm 0.02$  and this has been confirmed by many other simulations and real experiments since then (Jullien and Botet, 1987). It is argued that  $D$  is a universal scaling constant for such structures, although as we noted in the last chapter, there are other theorists such as Muthukumar (1983) who argues that  $D = (E^2 + 1)/(E + 1)$ , where  $E$  is the dimension of the space: when  $E = 2$ ,  $D = 1.66$ . No way has yet been found to predict  $D$  theoretically. In the previous chapter, we showed that  $D$  was nearer 1.66 than 1.70, but there is recent speculation and some evidence that  $D$  depends on the size of the lattice and the number of particles constituting the cluster as well as the methods used to estimate this parameter (Meakin and Tolman, 1989). Meakin (1986b) who has produced extensive simulations of DLA also argues that the geometry of the underlying lattice has an effect on the shape of the growing cluster (Meakin, 1986c).

Although the usual model of DLA is based on algorithms which simulate the random walk, the original statement of the model by Witten and Sander (1983) was presented in more formal terms as follows. On a square lattice whose coordinates are given as  $(x, y)$ , the probability of a walker visiting point  $(x, y)$  at time  $t$ , given by  $u(x, y, t)$  is

$$u(x, y, t) = \frac{1}{4} [u(x + 1, y, t - 1) + u(x - 1, y, t - 1) + u(x, y + 1, t - 1) + u(x, y - 1, t - 1)]. \quad (8.1)$$

Rearranging equation (8.1), we get

$$[u(x + 1, y, t - 1) - 2u(x, y, t) + u(x - 1, y, t - 1)] + [u(x, y + 1, t - 1) - 2u(x, y, t) + u(x, y - 1, t - 1)] = 0. \quad (8.2)$$

Equation (8.2) is a discrete approximation to the continuum limit of the Laplace equation

$$\frac{\partial u(x, y, t)}{\partial t} = \frac{\partial^2 u(x, y, t)}{\partial x^2} + \frac{\partial^2 u(x, y, t)}{\partial y^2} = 0, \quad (8.3)$$

which can be more generally stated as

$$\frac{\partial u(x, y, t)}{\partial t} = \phi \nabla^2 u(x, y, t), \quad (8.4)$$

where  $\phi$  is the diffusion constant. Note that we can assume that equations (8.3) or (8.4) are equal to zero (or a constant) because the source of diffusion is far away, the walk of each particle is slow, and the emission of particles is uniform. It is also clear that the growth velocity  $v(x, y, t)$  of any site is

$$v(x, y, t) = \nabla u(x, y, t), \quad (8.5)$$

and that growth is subject to the following boundary conditions. On the interface between the edge of the cluster and the lattice, that is, for those particles forming the boundary of the cluster, there is zero probability of

reaching these sites,  $u(x, y, t) = 0$ . This simply rules out the already developed cluster from reoccupation. At the distant source, the probability of reach is 1, that is  $u(x, y, t) = 1$ , for this is the source of the walkers. The model can then be solved from equation (8.4) subject to these two boundary conditions. Further details are given in the review paper by Witten (1986).

The DLA model provides a remarkable analog for a range of physical diffusion problems such as the diffusion of viscous fluids and dielectric breakdown, and there is very clear evidence that the model is applicable to these real physical processes (Ball, 1986). For viscous fluids, the applicability of DLA was first noted by Paterson (1984) for a process in which a fluid with low viscosity replaces one with high viscosity through permeation. Here  $u(x, y, t)$  is the velocity potential, the equation of fluid flow  $v(x, y, t)$  embodies Darcy's law, and the Laplace equation is the incompressibility condition. A variety of such simulations are noted in the paper by Nittmann, Daccord and Stanley (1985). However, the most useful model for generating a continuum of forms is the dielectric breakdown model (DBM) first presented by Niemeyer, Pietronero and Wiesmann (1984) which we refer to here as the continuum model.

In this model, the probability field  $u(x, y, t)$  of the DLA model is now a potential electric field,  $\phi(x, y, t)$ . The central seed site is the point of discharge in the field; its potential  $\phi(x, y, t) = 0$ , and the breakdown occurs in the direction of the highest potential in the field,  $\phi(x, y, t) = 1$ , which is the uniform attractor at a distance far from the source. The model thus simulates the breakdown of the field and produces dendritic structures characteristic of, for example, lightning amongst other forms. The probability that any site adjacent to the discharge pattern created so far will form the next point of discharge, is analogous to the flow modeled by equation (8.5), that is

$$p(x, y, t) = \frac{\frac{\partial\phi(x, y, t)}{\partial x} + \frac{\partial\phi(x, y, t)}{\partial y}}{\sum \left( \frac{\partial\phi(x, y, t)}{\partial x} + \frac{\partial\phi(x, y, t)}{\partial y} \right)} \quad (8.6)$$

where the summation is over all candidate sites adjacent to the pattern of discharge. The partial derivatives in equation (8.6) reduce to  $\phi(x, y, t)$  for all the candidate sites, because the potential at the interface is zero. This is the boundary condition equivalent to that on the edge of the cluster generated by the DLA model.

The DBM model is thus solved from Laplace's equation as

$$\nabla^2\phi(x, y, t) = 0, \quad (8.7)$$

subject to the boundary conditions  $\phi(x, y, t) = 0$  at the interface between the discharge and the field, and  $\phi(x, y, t) = 1$  for those potential points which are at distance  $r > R_r$ , where  $r = [(x - x_c)^2 + (y - y_c)^2]^{\frac{1}{2}}$ , and  $R_r$  is a distance threshold.  $x_c$  and  $y_c$  represent the coordinates of the central point of discharge. This model is formally equivalent to the DLA model sketched previously. It leads to fractal structures which are simply-connected dendrites which in turn form the patterns of discharge. Moreover, the Laplace equation in equation (8.7) ensures that the field is non-local and the

boundary condition at the edge of the cluster or discharge ensures that this field continually adapts to the increasing discharge.

The most innovative feature of DBM, however, relates to the way in which the field,  $\phi(x, y, t)$ , can be systematically distorted. Niemeyer, Pietronero and Wiesmann (1984) show that different forms of discharge can be predicted if the probability of discharge in equation (8.6) is scaled by means of a parameter  $\eta$ . We will define the potential as  $\phi_{x,y}$ , suppressing time  $t$ . The probability of growth at the interface,  $p_{x,y}$ , is now given as

$$p_{xy} = \frac{\phi_{x,y}^\eta}{\sum_{x,y \in C} \phi_{x,y}^\eta}, \quad (8.8)$$

where the summation is over all those sites  $(x, y)$  which are part of  $C$ , the interface to the pattern of discharge at time  $t$ . Before we show how the form is affected by the parameter  $\eta$ , we will summarize the classic case where  $\eta = 1$ . In Figure 8.1, the lattice on which the discharge takes place is illustrated with the solid dots and bonds showing the pattern of discharge so far, and the open dots and broken bonds showing the sites adjacent to the discharge for which the probabilities of selection are computed as in equation (8.8). Niemeyer, Pietronero and Wiesmann (1984) compute the fractal dimension of DBM as  $D = 1.75 \pm 0.02$ .

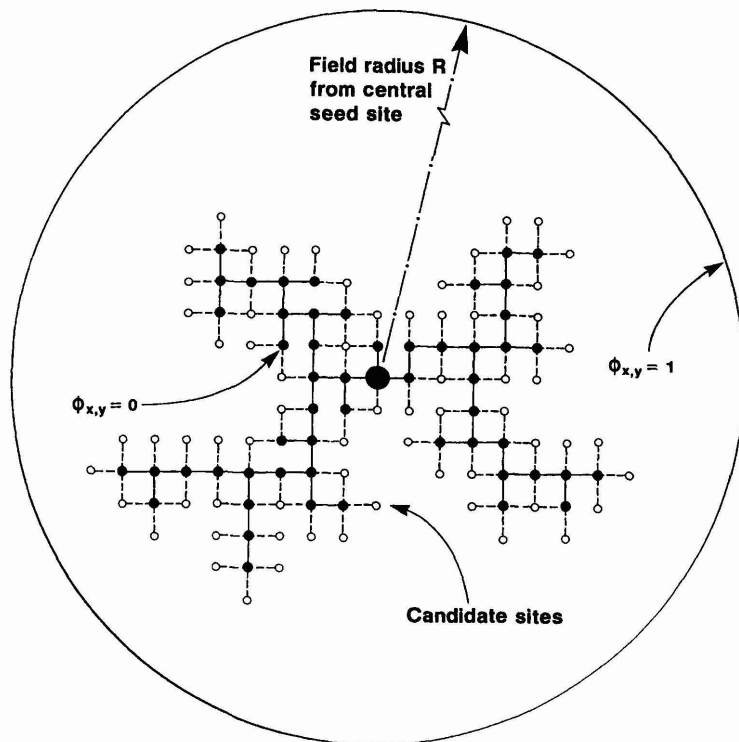


**Figure 8.1.** Cluster growth on a square lattice.

## 8.3 Analogies and Solutions

Comparisons with existing diffusion models of urban location which have developed as a part of social physics are instructive. Diffusion usually occurs from points of higher to lower potential, the highest point being the central site or CBD in the case of a city. Population potential as suggested by Stewart and Warntz (1958) is sometimes used to define a field analogous to gravitational potential, and diffusion thus takes place according to geographical distance decay, sometimes combined with a local or neighborhood effect (Hagerstrand, 1965). The DLA model is quite different. The highest potential is farthest away from the central site, and once a site has been occupied, its potential for reoccupation is zero. In fact, the potential measures the amount of space available at a distance from the central seed site and this captures the notion that it is the environment around a city which is the source of growth, not the city itself.

However, the city grows by finding areas of highest potential adjacent to existing development, and this constrains the development to remain as a connected aggregate. The DLA model is a less useful analog than DBM because the process of random walking is less realistic than the discharge process with respect to urban form. As Nittmann, Daccord and Stanley (1986) also state: "DLA has the purely phenomenological drawback that the cluster growth occurs by aggregation, whereas in RVF [radial viscous fingering], growth originates from the center of the structure". It is useful to think of the potential function  $\phi(x, y, t)$  as reflecting available space in the immediate vicinity of the site  $(x, y)$  but also influenced by the growing cluster. In this sense, it is clear that the branch tips of the cluster are 'closest' to the points of highest potential, and it is easy to see why growth would occur there, thus reinforcing the dendritic nature of the structure. Once sites are occupied they have no further space potential, and this ensures the irreversibility of the process. Moreover, the basic constraint that the cluster must remain connected enables the process to be one of balancing the achievement of maximum space potential against the need to generate the scale economies associated with a connected spatial cluster.

The concepts of flow and potential appear extensively in social physics, but the restrictive nature of the Laplace equation governing the smoothness of the potential field has not been widely invoked. In fact, Sheppard (1979) suggests that the general form of Poisson's equation where  $\nabla^2\phi(x, y, t) = g(x, y, t)$ , is more appropriate,  $g(x, y, t)$  representing some local source of variation at  $(x, y)$ . Tobler (1981) and Dorigo and Tobler (1983) have used Poisson's equation in their models of movement, where  $g(x, y, t)$  represents differences in spatial attraction. In modeling migration, Dorigo and Tobler minimize  $\nabla^2\phi(x, y, t)$  to derive migration potentials and flows, and it is possible that a related interaction-flow interpretation might be given to DLA and DBM. In fact, Niemeyer, Pietronero and Wiesmann (1984) note that a length scale can be introduced into the simulation if  $\nabla^2\phi(x, y, t)$  is assumed to be a positive constant over all  $(x, y)$ . However, it is probably more useful to think of the Laplace equation as imposing a smoothness criterion across the field which balances local and global effects. This

interpretation has also been exploited by Tobler (1979a) in modeling general geographic fields.

We can now speculate on the continuum of urban forms which might be generated using DBM through equations (8.7) and (8.8). The fractal case,  $\eta = 1$ , can be regarded as the baseline where the spatial potential function remains undistorted. As  $\eta \rightarrow 0$ , the sites which might be occupied around the boundary of the cluster become more evenly distributed, with the implication that the cluster will grow in a much less branch-like fashion. When  $\eta \gg 1$ , structures based on lines of particles across the space will emerge, and the implication is that the fractal dimension  $D$  will tend towards 1. In other words, 'linear cities' will be generated for  $\eta \gg 1$ , dendrites for  $\eta = 1$ , and circular cities for  $0 \leq \eta \ll 1$ . A continuum of forms will emerge where the parameter  $\eta$  in the range 0 to  $\infty$  maps onto the range of fractal dimension  $D$  from 2 to 1.

There is one last speculation to be made before the discrete form of the model is discussed. The parameter  $\eta$  which distorts the potential field  $\phi_{x,y}$  might be regarded as a measure of 'planning control'. To produce linear cities, certain sites have to be given exclusive preference for development and this can only occur if planning control is absolute and the market for land is in the hands of a single agent. At the other extreme, where there is a different type of control, the market might consist of many agents each bidding for development sites. This is consistent with a city which grows amorphously. The extremes of the linear and amorphous cities reflect the parameter values from  $\eta \rightarrow \infty$  and  $\eta \rightarrow 0$ , respectively. The baseline case where  $\eta = 1$  thus consists of a few large land agents and many small ones, thus mirroring the kind of markets that might characterize Western industrialized cities. To go further with this speculation would not be wise, but in general it fruitful to think of  $\eta$  as embodying a measure of planning control.

The major disadvantage to formulating the model in DBM rather than DLA terms relates to its solution. For each additional particle which is added to the cluster, the Laplace equation (8.7) must be solved subject to the previously given boundary conditions. For a lattice of  $500 \times 500$  points say, there are up to 250,000 non-linear partial differential equations to be solved. These can only be solved iteratively and experience suggests it takes at least ten iterations to effect a solution. Where there is a cluster of 10,000 particles to be grown, this will involve the solution of 25 billion equations. In terms of computer time the problem is likely to take ten times as long as its equivalent formulation as a DLA model, thus requiring amounts of supercomputer time simply not available for these experiments. However, the model must be solved in DBM terms if the effects of varying the control parameter  $\eta$  are to be evaluated. Consequently smaller lattices will be used for growing particle clusters, in contrast to those demonstrated previously for the DLA model in Chapter 7.

The discrete approximation to Laplace's equation will now be restated, with the time subscript  $t$  omitted. Then

$$\phi_{x,y} = \frac{1}{4}(\phi_{x+1,y} + \phi_{x-1,y} + \phi_{x,y+1} + \phi_{x,y-1}). \quad (8.9)$$

Equation (8.9) can be generated as an approximation based on forward differences, and, for any iteration of its solution, the difference between the right-hand and left-hand sides of equation (8.9) is given as

$$\Phi_{x,y} = \phi_{x,y} - \frac{1}{4}(\phi_{x+1,y} + \phi_{x-1,y} + \phi_{x,y+1} + \phi_{x,y-1}). \quad (8.10)$$

The method of solution used to solve equation (8.9) involves identifying the differences  $\Phi_{x,y}$  across the lattice, and relaxing values of  $\phi_{x,y}$  according to the largest differences adjacent to each point  $(x, y)$  (Williams, 1987). In the simulations to be reported here, once the original potential field  $\phi_{x,y}$  has been computed at time  $t = 0$ , it takes an average of 13 iterations of equation (8.9) to bring each potential value  $\phi_{x,y}$  to within 0.5% of its averaged neighboring values. Formally, the iteration on equation (8.9) (and (8.10)) using relaxation methods ceases when

$$\max_{(x,y)} \frac{\Phi_{x,y}}{\phi_{x,y}} \leq 0.005. \quad (8.11)$$

At each time  $t$ , once the field  $\phi(x, y, t)$  has been computed to the criterion set in equation (8.11), the probabilities of the candidate sites adjacent to the cluster are computed from equation (8.8), and one is selected for growth using a randomly generated number. This changes the boundary condition on the interface which in turn necessitates that the field  $\phi(x, y, t)$  be recomputed, and so the process continues until the cluster has been grown to the required size.

The structures generated by the continuum model do of course follow the same scaling laws as those used to describe the distribution of particles in the DLA model regardless of the values of the parameter  $\eta$ . The four scaling relations linking the size characteristics of the cluster to the radial distance  $R$  from the cluster's center are those which relate  $N(R)$ ,  $dN(R)/dR$ ,  $\rho(R)$ , and  $dN(R)/d\hat{A}(R) (= Q(R))$  to  $R$ , given previously as equations (7.23), (7.24), (7.25) and (7.26), in that order.  $N(R)$  is the cumulative count of the particle or population,  $dN(R)/dR$  the actual population at  $R$ , which as Pietronero, Evertsz and Wiesmann (1986) note, gives the number of branches or bonds in the discharge pattern or cluster at a given distance,  $\rho(R)$  is the cumulative density, and  $dN(R)/d\hat{A}(R)$  is one measure of the actual density at  $R$ . The parameters of these relations are all simple functions of the fractal dimension  $D$ , easily computed through logarithmic regression as in Chapter 7.

The discrete measures used for the dependent variables in each of these relations are of two forms: either a simple count of the number of particles and their density with respect to the central seed site, these being known as one-point measures; or averages of the same counts but taken over all possible sites in the cluster, these being the two-point measures. The computation of these one-point measures is given in equations (7.27) to (7.33) and the two-point measures in (7.34) to (7.40), and we will make use of these equations again in this chapter. The one-point measures for fixed distance bands  $R$  are defined as  $N(R)$ ,  $\Delta N(R)$ ,  $\rho(R)$  and  $Q(R)$  and, as in Chapter 7, the two-point measures are notated similarly with bars indicating that these are averages, that is  $\bar{N}(R)$ ,  $\Delta\bar{N}(R)$ ,  $\bar{\rho}(R)$  and  $\bar{Q}(R)$ .

The use of two-point averages is standard practice as approximations to density-density correlation functions (Meakin, 1986b; Witten and Sander, 1983), and both two-point and one-point measures can be used to find the parameters of the scaling relationships given in equations (7.23) to (7.26). In logarithmic form, these relations, given in equations (7.49), are repeated here for convenience as

$$\left. \begin{aligned} \log N(R) &= \alpha_1 + \beta_1 \log R, \\ \log n(R) &= \alpha_2 + \beta_2 \log R, \\ \log \rho(R) &= \alpha_3 + \beta_3 \log R, \\ \log Q(R) &= \alpha_4 + \beta_4 \log R. \end{aligned} \right\} \quad (7.49)$$

Note that one-point measures are stated here, and it is assumed that the distance bands associated with  $R$  are equal. Last, the fractal dimensions can be computed from the slope parameters in equations (7.49) as  $D = \beta_1$ ,  $D = 1 + \beta_2$ ,  $D = 2 + \beta_3$ , and  $D = 2 + \beta_4$ , respectively. Use of the two-point measures, however, is a problem because of the computer time involved, and the use of regression analysis is extremely sensitive to the range of distance bands selected. It is well known that these occupancy and density functions are highly variable over a short range in the vicinity of the origin, and there are marked edge effects over the larger scale because of the fact that the clusters are still developing in a wide area of their periphery. Regression analysis is able to cope well with these edge effects, but it is difficult to identify the short-range effects. This suggests the need for both faster and more robust methods of estimation which we briefly presented in the last chapter. As these methods are used widely in this chapter, we will restate them.

As all measurements and simulations take place on a square lattice with unit spacing, it is expected that  $N(R) \sim \pi R^D$ , and  $\hat{A}(R) \sim \pi R^2$ . Therefore the density in equation (7.25) can be specified as

$$\rho(R) = \frac{N(R)}{\hat{A}(R)} \sim R^{D-2}. \quad (8.12)$$

For any value of  $R$ , it is thus possible to count  $N(R)$  and measure  $\hat{A}(R)$  and to manipulate equation (8.12) to provide an approximation to  $D$  which we will call  $D(R)$ . Then

$$D(R) \sim 2 + \frac{\log \rho(R)}{\log R}. \quad (8.13)$$

In a real example or typical simulation, we are likely to have a very large number of values of density associated with distances  $R$ , and from the first distance  $R = r$  to the boundary of the cluster where  $R = R_m$ , we can compute values of  $D(R)$ . For example, if we begin at the seed site and measure density  $\rho(R)$  with increasing distance from this center, we might expect  $D(R)$  to be volatile over the short range in the vicinity of the seed site but to settle down gradually as the cluster grows outwards. Towards the edge of the cluster, a change in  $D(R)$  may occur, thus revealing that this is still an area of growth and that the cluster is incomplete.

A plot of  $D(R)$  against  $R$  will reveal the stability of the dimension, and we will refer to this somewhat loosely as the 'signature' of the fractal cluster. We might expect different fractal forms to exhibit different signatures, but as yet, we still have to explore this possibility. However, we would expect  $D(R_m)$  to be a biased estimate of  $D$  for this pertains to the entire cluster. A more appropriate value of  $D$  for the cluster would be  $D(\bar{R})$ , where  $\bar{R}$  is the mean distance about the seed site in the cluster, defined as

$$\bar{R} = \frac{1}{N} \sum_{r=R_0}^{R_m} \bar{n}(r)r, k = 1. \quad (8.14)$$

The seed site or center of the cluster is at  $k = 1$ , and  $R_0$  represents the first distance for which occupancy around the seed site occurs.

This fast estimation procedure given in equation (8.13) is possible because the constants of proportionality defining the scaling relations cancel. It is possible to construct other measures which normalize estimation in this fashion, and we will note two. First we can normalize equation (7.23) as

$$\frac{N(R)}{N(R_m)} = \left( \frac{R}{R_m} \right)^D, \quad (8.15)$$

from which  $D_N(R/R_m)$  can be estimated as

$$D_N(R/R_m) = \frac{N(R)}{N(R_m)} / \log \left( \frac{R}{R_m} \right), \quad (8.16)$$

In a similar manner, the same can be done for density in equation (7.25). Then

$$\frac{\rho(R)}{\rho(R_m)} = \left( \frac{R}{R_m} \right)^{D-2}, \quad (8.17)$$

from which  $D_\rho(R/R_m)$  can be predicted as

$$D_\rho(R/R_m) = 2 + \left[ \frac{\rho(R)}{\rho(R_m)} / \log \left( \frac{R}{R_m} \right) \right]. \quad (8.18)$$

We will use equations (8.16) to (8.18) below, but to anticipate our conclusions, equation (8.13) is the most useful estimation technique found so far.

## 8.4 Form and Dimension of the Baseline Model

Our previous simulations with the DLA model used a square lattice of  $500 \times 500$  points and grew clusters of 10,000 particles achieving an average density of occupation of the lattice of 4%. These simulations each took 10 hours of CPU time on a MicroVax which was dedicated to these runs. To solve the continuum model at the same level of resolution and cluster size would take at least 12 days. Although supercomputer facilities were available, the amount of supercomputer time required was too great, and the only way to proceed was to work with coarser lattices and smaller clusters. As an example, we will first show a simulation of the DBM for a  $300 \times 300$  lattice with a cluster size of 4157 particles. This simulation took one day, 21 hours and two minutes CPU time on the MicroVax, and thus in the more extensive analysis following this section we were forced to reduce the resolution of the lattice even further to  $150 \times 150$  so that CPU time could be contained within five hours or so for each simulation run.

As already reported, the model was solved by iterating equations (8.9) to (8.11) for each time period and randomly allocating particles to lattice sites according to the probabilities given in equation (8.8) with  $\eta = 1$ . The number of particles generated in the examples reported here was not fixed in advance, for each cluster was grown up to about two thirds of the maximum radius of the lattice, which for a  $300 \times 300$  lattice with the seed site fixed at  $x = y = 150$ , is  $R_m = 100$ . In this case, the model generates a cluster of 4157 particles. As  $\eta$  changes, however, the number of particles will change because  $\eta$  controls the compactness and density of the cluster. The other critical issue which affects the simulations involves the location of the outer boundary defining the highest points of potential. This boundary is fixed at the maximum radius of the lattice, in the case of the  $300 \times 300$  lattice, at  $R_{\max} = 150$ . Thus the cluster is grown two thirds of the way towards this boundary. In the experiments reported, it would appear that the cluster is not distorted with  $R_{\max}$  set at  $\frac{3}{2} R_m$  or greater. We have examined the smoothness of the field as the cluster grows and it seems that the isotropy of the field outside the cluster is maintained. However, we are conscious that we are working at the limits of acceptable cluster growth and this problem can only be resolved by running the model on an appropriate supercomputer.

The forms produced by this simulation are shown in Figures 8.2 and 8.3. Figure 8.2 shows the way sites are selected in the cluster with respect to their bonding to the various occupied lattice points. This clearly reveals the dendritic structure as in Figure 8.1 and it is obvious that the graph of this structure is simply connected. Figure 8.3 shows the order or dynamics in which sites are occupied. Twelve gray scales are used to show this order with the darkest sites being the earliest to locate, the lightest the latest; because of difficulties in capturing these images photographically and reproducing the gray scales, this and other similar figures are impression-

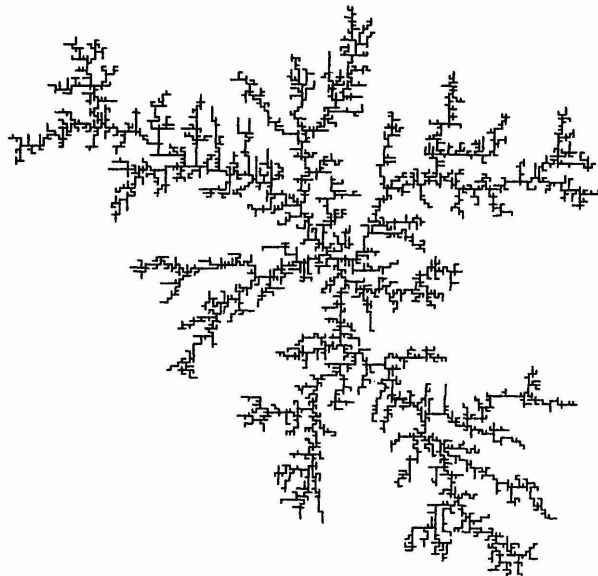


**Figure 8.2.** Dendritic fractal growth as a simply connected graph.



**Figure 8.3.** A system history of fractal growth using the continuum model.

istic, but nevertheless this does provide a clear illustration of the history of the system. Comparison of Figures 8.2 and 8.3 also shows that the dendritic pattern in Figure 8.2 is blurred by the coloring in Figure 8.3, thus leading to some cells appearing as though they are surrounded.

The structural characteristics of urban form will be measured using various indices of size and density. The total number of lattice points,  $N_L$  is 90,000, that is  $300 \times 300$ . The number of points occupied is given as  $N$  and the density  $N/N_L$  reflects the degree of sparseness of the structure.  $R_{\max}$  the maximum radius of the lattice,  $R_m$  the maximum radius of the cluster ( $\approx 0.66R_{\max}$ ), and  $\bar{R}$  the mean distance within the cluster have already been defined. Three other measures describe the compactness of the structure. First the average density is defined as

$$\rho = \frac{N}{\pi R_m^2}.$$

The number of particles on the boundary of the cluster can be counted directly as  $N_b$  and the ratio of boundary to total occupied points defined as

$$\vartheta = \frac{N_b}{N}.$$

The proportion of interior points in the cluster is then  $1 - \vartheta$ . The last measure of consequence is the average number of nearest neighbors defined as

$$\xi = \frac{N_n}{N'}$$

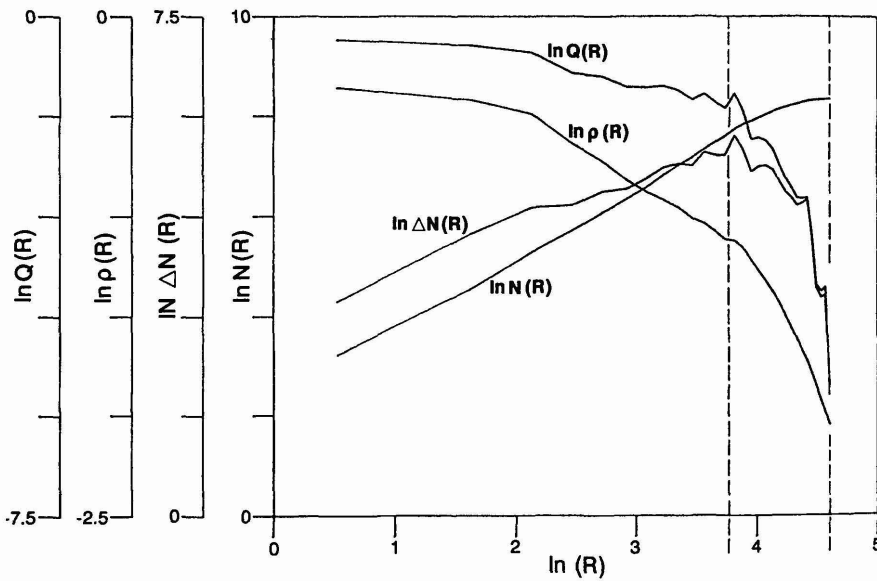
where  $N_n$  is the total number of nearest neighbors for all particles in the system; each particle has eight possible neighbors according to the eight compass points around the point in question on the lattice.

Table 8.1 presents these various measures for the  $300 \times 300$  lattice example simulated here, and the  $150 \times 150$  lattice model presented in the next section. These models will be referred to henceforth as the baseline models. These will act as a basis for comparison when the potential field is distorted and when areas of the lattice are absent from the spatial system. This table is largely self-explanatory. However, it is worth noting that the lattice density  $N/N_L$  and the average density  $\rho$  decline as the system gets larger. This is an obvious consequence of the model and is consistent with the density in equation (7.25) which embodies a negative fractional power law. In later comparisons where the lattice is of the same size, variations in these densities will become relevant. The boundary ratio  $\vartheta$  is slightly less than 1, despite the fact that Figure 8.2 reveals that all the particles are on the boundary of the structure. This is simply a consequence of the way the boundary is represented which is as in Figure 8.3, not Figure 8.2. Lastly, the average number of nearest neighbors can range from 0 to 8 and this represents a measure of the compactness of the structure.

The parameters which give rise to different dimensions  $D$  are a function of the four power laws given in equations (7.23) to (7.26). These equations can be linearized as in equations (7.49) and parameters  $\beta_1$ ,  $\beta_2$ ,  $\beta_3$  and  $\beta_4$  estimated using regression analysis. The fractal dimensions are derived as  $D = \beta_1$ ,  $D = 1 + \beta_2$ ,  $D = 2 + \beta_3$  and  $D = 2 + \beta_4$ , and these can be computed for two sets of measures; the one-point (or two-point measures)  $N(R)$ ,  $\Delta N(R)$ ,  $\rho(R)$  and  $Q(R)$  are then used in their respective regressions. We will begin with the one-point measures, and these are plotted in their logarithmic form in Figure 8.4. The edge effect posed by the incompleteness of the cluster is easily detectable, but identifying the short-range effect is much more problematic. These graphs are based on dividing the range of distance up to  $R_m$  into 30 distance bands where each band is of equal width  $R_m/30$ .

**Table 8.1.** Characteristics of the baseline model

System characteristic	Fine resolution baseline	Coarse resolution baseline
Dimension	$300 \times 300$	$150 \times 150$
Lattice points, $N_L$	90,000	22,500
Occupied points, $N$	4157	1856
$N/N_L$	0.046	0.082
Lattice radius, $R_{max}$	150	75
Cluster radius, $R_m$	101.356	49.366
$R_m/R_{max}$	0.676	0.658
Mean distance, $\bar{R}$	45.734	27.183
$\bar{R}/R_m$	0.451	0.544
Average density, $\rho$	0.129	0.236
Boundary ratio, $\vartheta$	0.957	0.959
Nearest neighbors, $\xi$	4.943	4.862



**Figure 8.4.** Logarithmic one-point functions.

These plots in Figure 8.4 are very similar to their respective plots for the DLA simulation shown in the previous chapter. Table 8.2 presents the dimensions  $D$  computed from each regression estimate, the standard errors of the regression slope coefficients, and the  $r^2$  goodness-of-fit statistics. The first results are poor; these are then reestimated taking out the long-range effects by restricting the data to the first 13 distance bands. Although the standard errors and  $r^2$  statistics improve dramatically in every case, the variation in dimension from  $D = 1.376$  to  $D = 1.737$  indicates that it is the method of estimation which is volatile with respect to the functions fitted and the data used.

The equivalent two-point functions are plotted in Figure 8.5. These are widely regarded as being better measures to be used in estimation, and the functions are clearly much smoother, being formed from averages of points associated with all distinct distances within the lattice. These functions

**Table 8.2.** One-point estimates for the fine resolution model

Distance bands	$D = \beta_1$	$D = 1 + \beta_2$	$D = 2 + \beta_3$	$D = 2 + \beta_4$
1-30	1.317	0.994	1.554	0.994
	0.023	0.166	0.038	0.166
	0.991	0.000	0.834	0.568
1-13	1.376	1.660	1.737	1.660
	0.019	0.031	0.023	0.031
	0.998	0.997	0.916	0.917

*Note:* the first line of results for each distance band gives the fractal dimension, the second line the standard error, and the third the adjusted coefficient of determination  $r^2$ . These definitions are used for all subsequent tables of this type in this chapter.

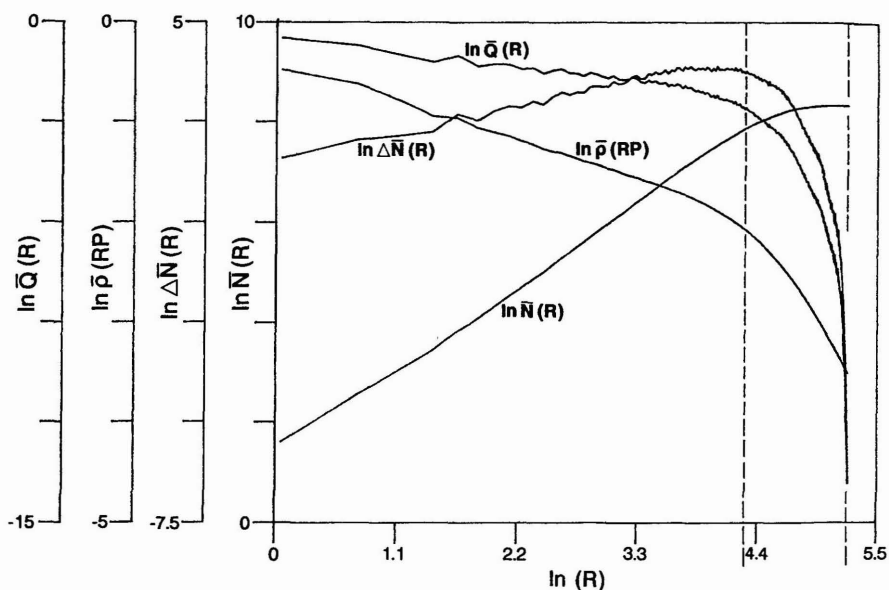


**Figure 8.5.** Logarithmic two-point functions.

appear similar to those computed in the last chapter for the DLA model. There are 187 distinct distance bands and, again, the long-range edge effect is clear. The first regressions shown in Table 8.3 are for all these distance bands, and the results are poor. Restricting the estimation to the first 55 distances improves the performance dramatically, but the fractal dimensions vary between 1.537 and 1.646, again suggesting that the methods of estimation are unreliable. It is quite clear that the regression methods are too sensitive to the functions used, and the data averages and aggregations made. There is need for a simpler, more robust method of estimation, and we will use that which we introduced earlier in equations (8.12) to (8.16). First, equation (8.13) has been plotted for  $R$  up to  $R_m$ , the cluster radius, thus producing a 'signature' of the form shown in Figures 8.2 and 8.3. This in effect is a cumulative computation of the fractal dimension  $D$  from the center to the edge of the cluster, and it is shown in Figure 8.6. It is quite clear that this signature is extremely volatile in the vicinity of the origin or center site and that once it settles down, the fractal dimension  $D$  is virtually

**Table 8.3.** Two-point estimates for the fine resolution model

Distance bands	$D = \beta_1$	$D = 1 + \beta_2$	$D = 2 + \beta_3$	$D = 2 + \beta_4$
1-187	1.257	0.005	1.311	0.058
	0.019	0.143	0.021	0.134
	0.959	0.258	0.853	0.533
1-55	1.537	1.588	1.646	1.588
	0.007	0.012	0.003	0.012
	0.999	0.977	0.996	0.954

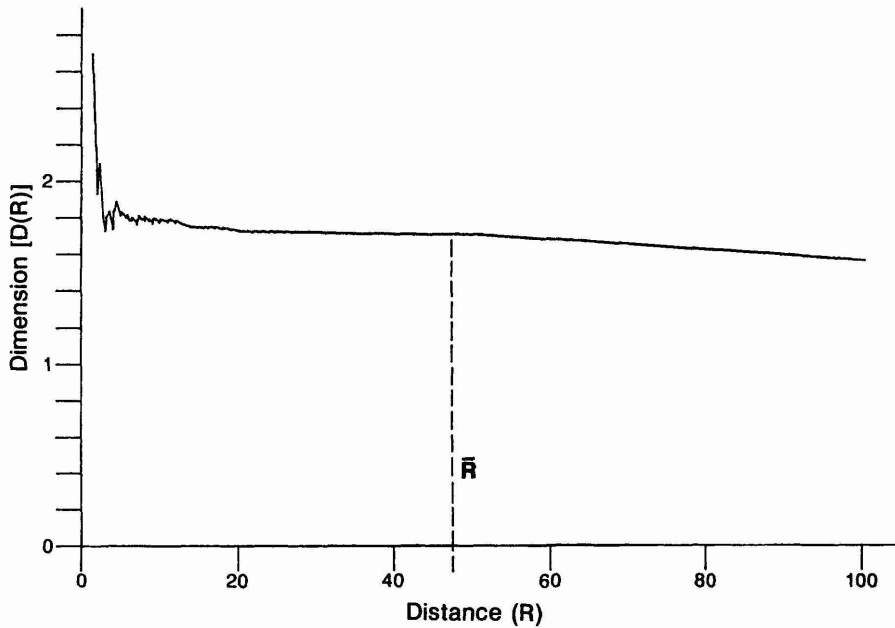


**Figure 8.6.** The fractal signature of the fine resolution baseline model.

constant over most of the cluster, beginning to fall as the incomplete area at the edge of the cluster is approached. From Figure 8.6, it is immediately clear that a good estimate of  $D$  is obtained at the mean distance  $\bar{R}$ .

At  $\bar{R}$ ,  $D(\bar{R}) = 1.708$  in comparison with  $D(R_m) = 1.556$  at the edge of the cluster. It is also possible to form the average of all the dimensions  $D(R)$  up to  $R_m$ , and this gives  $D = 1.681$ , biased towards the value of 1.708, an approximation to this value prevailing over most of the radius of the cluster. In Figure 8.6, the range of  $D(R)$  is from 2.697 to 1.556, where  $R$  varies from 1.414 to 101.356, the cluster edge. By the time  $R$  has reached 13.342, the dimension has fallen to 1.756, indicating that the appropriate dimension of the cluster is about 1.7. This is close to the universal value of 1.71, and as we shall see, it is a remarkably robust procedure for determining such values. Last, we will examine the dimensions produced using equations (8.16) and (8.18). We can compute signatures based on these equations, but these appear to give values of  $D$  which are too low. For example,  $D_N(\bar{R}/R_m) = 0.829$  and a similar value is given for  $D_\rho(\bar{R}/R_m)$ . In fact, the edge of the cluster is not a good basis for estimation, and thus in future examples, we will restrict the estimation to the use of equation (8.13) in plotting the signature of the form and to  $\bar{R}$  in determining the most appropriate fractal dimension.

## 8.5 The Effect of Randomness on Form and Dimension

Before we begin to demonstrate how the control parameter  $\eta$  can generate very different forms of structure, we need to investigate two features of

the simulation which affect its fractal dimension. In this section, we will explore the effect of randomness on the model, and in the next, we will investigate how reducing the lattice space available for growth alters the fractal dimension and constrains urban form. The field equations which enable the potential  $\phi_{x,y}$  to be evaluated define the probabilities that the candidate sites on the boundary of the cluster will receive growth. Whether or not one of these candidate sites receives a unit of development in the given time period depends upon the random number generated. In this sense, then, the resultant cluster, although structured in the large according to the potential field, develops in the small through random decision-making. Each run will thus yield a different form, although it is hoped that variations in these forms will have little effect on their dimension. It is this that we will explore in this section. To do so effectively, we require a large number of runs of the model, say at least 30, and this would require about two months of computer time were we to use the fine resolution model. Therefore we will compute a new coarse resolution model based on a  $150 \times 150$  lattice which will henceforth act as our baseline.

The physical characteristics of this model have already been listed in Table 8.1. The urban form produced will not be shown in this section, but readers who wish to view this now can find it in Plate 8.1 (see color section). The structure is quite similar to that in Figures 8.2 and 8.3. Its fractal dimensions have been estimated from both the one-point and two-point measures whose plots are similar to those shown earlier in Figures 8.4 and 8.5. The dimensions are listed for the one-point measures in Table 8.4 where the original 30-band distance data and the reduction to 20 bands to exclude long-range edge effects are shown. The two-point measures are shown in Table 8.5, and it is immediately obvious that the results are similar to those for the fine resolution baseline. In fact, the ranking of dimension values from the full and part one-point and two-point measures is identical to the ranking in Tables 8.2 and 8.3, and the final values produced in the part two-point measures in Table 8.5 are similar in absolute terms to those in Table 8.3. Similar comments with regard to the volatility of these methods to those made previously apply.

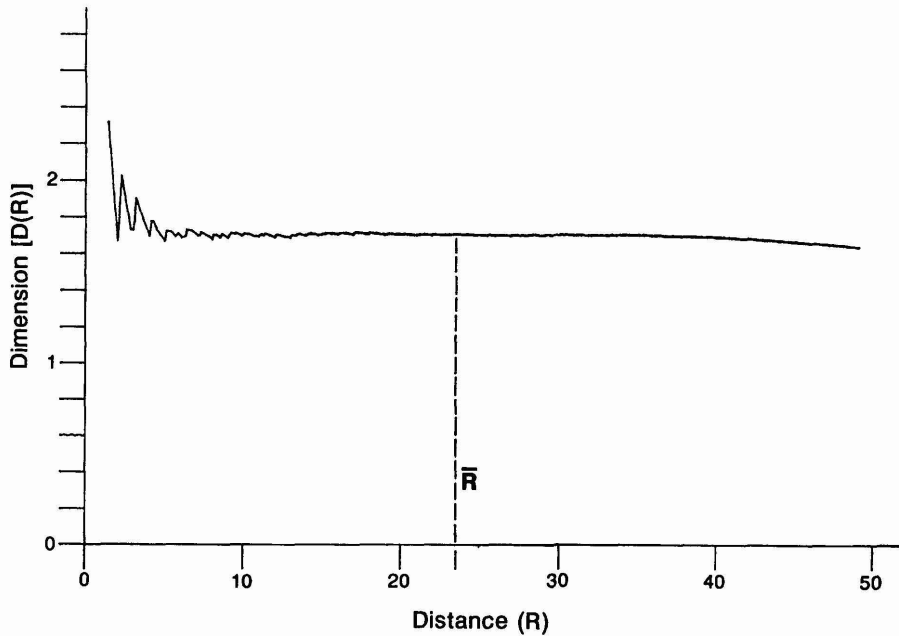
We have also used the fast method of estimation in which we first plot the signature of the model based on the graph of  $D(R)$  against  $R$  using equation (8.13). This is shown in Figure 8.7, and it is fairly similar to the signature of the fine resolution model shown in Figure 8.6: the short-range variation and long-range decline in  $D(R)$  are apparent, with  $D(R)$  varying

**Table 8.4.** One-point estimates for the coarse resolution model

Distance bands	$D = \beta_1$	$D = 1 + \beta_2$	$D = 2 + \beta_3$	$D = 2 + \beta_4$
1-30	1.467	1.431	1.704	1.431
	0.019	0.107	0.017	0.017
	0.995	0.368	0.917	0.503
1-20	1.458	1.718	1.751	1.718
	0.027	0.030	0.012	0.030
	0.994	0.970	0.960	0.833

**Table 8.5.** Two-point estimates for the course resolution model

Distance bands	$D = \beta_1$	$D = 1 + \beta_2$	$D = 2 + \beta_3$	$D = 2 + \beta_4$
1-98	1.311	0.219	1.390	0.219
	0.022	0.179	0.025	0.179
	0.974	0.165	0.862	0.508
1-34	1.504	1.602	1.644	1.602
	0.008	0.014	0.005	0.014
	0.999	0.982	0.994	0.960


**Figure 8.7.** The fractal signature of the coarse resolution baseline model.

from 2.312 for the first distance  $R$ , to 1.631 for  $R_m = 49.163$ .  $D(R)$  falls to 1.751 by  $R = 14.765$ , and the mean  $\bar{R}$  generates a value of  $D(R) = 1.701$ , about the same as that for the fine resolution cluster.  $D(R_m) = 1.631$  and the average over all  $D(R)$  generates 1.698. Last, the values of  $D_N(\bar{R}/R_m) = 1.251$  and  $D_\rho(\bar{R}/R_m) = 1.254$ . These confirm the comments made on these methods of estimation for the fine resolution model, and generate values of  $D(R)$  almost identical to those of other researchers (Feder, 1988; Jullien and Botet, 1987).

Including the model run just reported, we have made a total of 30 runs of the coarse resolution baseline model, seeding the random number generator with a random start value on each simulation. All the signatures produced mirror that in Figure 8.7 with similar volatility in the vicinity of the seed site and a gradual fall in dimension at the edge of the cluster. We have computed equation (8.13) for  $R_m$ ,  $\bar{R}$  and the average over  $D(R)$  for each run, and we have also formed the averages of these dimensions with

respect to all 30 simulations. In Figure 8.8, the frequency graphs of the dimensions produced are plotted, and it is clear that variation around the means of these dimensions is extremely narrow. The averages are as follows: for  $D(R_m)$ ,  $1.548 \pm 0.042$ ; for  $D(\bar{R})$ ,  $1.701 \pm 0.025$ ; and for  $D(\bar{R})$  averaged over the averages, the dimension is  $1.679 \pm 0.023$ . It is quite clear from Figures 8.6 and 8.7 that in this work, the most appropriate dimension to choose is based on the mean  $\bar{R}$ .

These values are also confirmed by other research. In the original statement of the model by Witten and Sander (1983),  $D = 1.70 \pm 0.02$ , and this was computed by averaging the results of six aggregates. Meakin (1986d) reports a value of  $D = 1.695 \pm 0.002$  over 500 aggregates for the DLA model, and he also reports that Stanley (1977) has estimated  $D = 1.715 \pm 0.002$  for 1000 runs of a 50,000 particle system. These simulations are all based on the DLA algorithm, although it is now clear that  $D$  is likely to vary according to the number of the particles and size of the system used (Meakin, 1986c). Nevertheless, comparison of Figures 8.6 and 8.7, as well as the frequencies

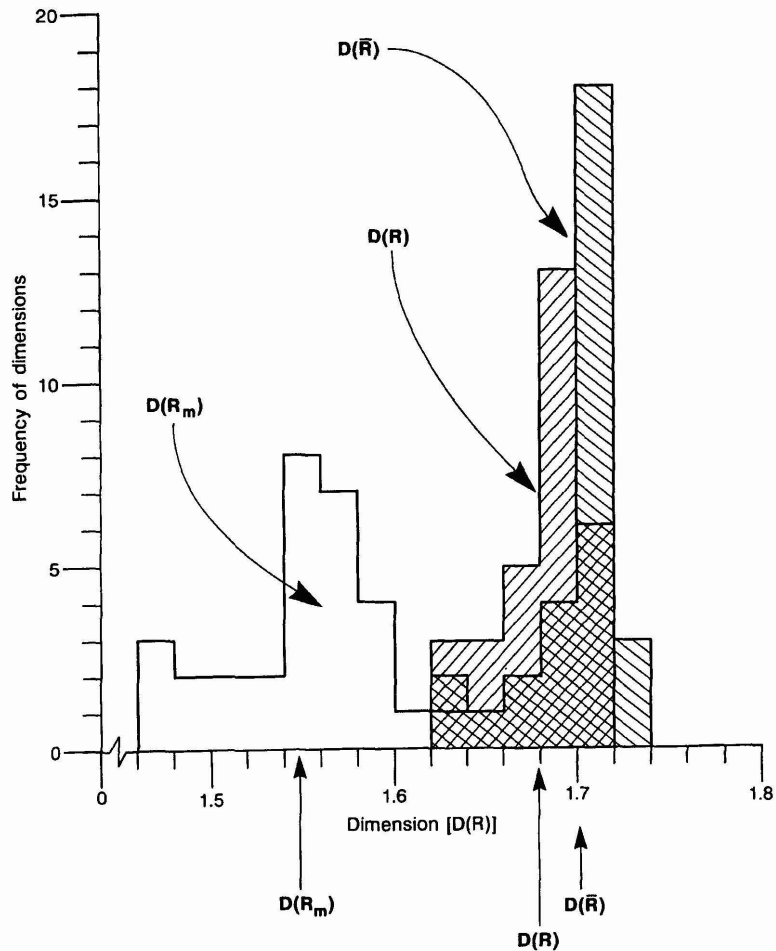


**Figure 8.8.** Frequency distributions of fractal dimension for the coarse resolution baseline model.

shown in Figure 8.8 does confirm the reliability of estimating fractal dimension from information on the mean occupancy,  $N(\bar{R})$  and density,  $\rho(\bar{R})$ .

## 8.6 Physical Constraints on the Simulation

Fractal dimension will clearly change as the control parameter varies from very small to very large positive values, but this dimension is also affected by the shape of the 'container' or lattice in which growth is initiated. If we begin with a circular field (on a square lattice) and systematically reduce its size by taking out larger and larger sectors, the growth of the cluster will be increasingly constrained or 'compressed' within the available space. In the limit, one might envisage that the excluded sector approaches the circle itself, and all that is left for the cluster to grow on is a line of lattice points. Thus the dimension of the cluster is likely to be progressively reduced from 1.7 to 1 in the case of the baseline model. This effect, however, is not as easily imagined as one might first think because it depends on the scale of the lattice. Fractals are self-similar across a range of scales, and although the lattice might be compressed at one scale, if the scale is magnified over many orders, a lattice would be reached which to all intents and purposes would not be so constrained. Measurement of the fractal dimension of the baseline model at this scale would then reveal no change from  $D = 1.7$ . This simply shows that, although we argue that fractal dimension is a measure of self-similarity across many scales, it is still dependent upon the finest scale available which in this context is the  $150 \times 150$  lattice.

A clear example of the effect of the 'container' on fractal dimension is provided by Nittmann, Daccord and Stanley (1985). These researchers set up an experiment to force a liquid of low viscosity into one of high viscosity using a Hele-Shaw cell whose geometry was a rectangle 10 units in length by three in width. The liquid of low viscosity entered the cell at the midpoint on its shorter side and the well-known fingers of liquid then began to spread through the cell. The estimated fractal dimension of the viscous fingering was  $D = 1.40 \pm 0.04$ , and Nittmann, Daccord and Stanley (1985) clearly show how the DBM style of simulation can generate a similar dendritic structure with a fractal dimension of  $D = 1.41 \pm 0.05$ . Other examples of growing clusters from edges rather than central points in space exist (Voss, 1984), and there is fairly wide agreement that, if the shape of the basic lattice is distorted, the fractal dimension will alter. There is some research by Kondo, Matsushita and Ohnishi (1986) who examine the relationship between the cluster grown in a wedge-shaped sector of varying angle  $\theta$ , and there is some discussion of the types of barrier used in such systems to absorb or reflect particles. However, these are for the DLA model. What follows here is a systematic examination of the effects of reducing the size of the space within which the DBM operates.

We will divide the circular plane into eight equal sectors, and proceed to apply the coarse resolution baseline model to the following degrees of arc:  $2\pi$  (the complete baseline model),  $1.75\pi$ ,  $1.5\pi$ ,  $\pi$ ,  $0.75\pi$ ,  $0.5\pi$  and  $0.25\pi$ . We thus move from a complete circular baseline simulation (the one

reported in the previous section) to a simulation based on a 45° wedge of the circle. It is important to note how the potential field is evaluated with respect to the lattice points which form the edges of these sectors. Equation (8.9) shows that the potential  $\phi_{x,y}$  depends upon an average of its four immediate neighboring potential values. If any of these potential values fall into the omitted sector, the potential average is then formed by excluding these values. In other words, the omitted sector is not treated as a boundary constraint but as a natural boundary to the system, outside of which no potential exists.

The forms produced by the simulations on these eight systems are shown in Plate 8.2, and it is immediately clear that the geometry of each system has a marked compressing effect on the growing clusters. In each of these clusters, we can measure physical characteristics of size and density as we have done previously in Table 8.1. Table 8.6 shows quite clearly that, as the degree of arc is progressively reduced and larger sectors are excluded, the lattice and average densities remain roughly the same. These densities range from 0.057 to 0.089 for  $N/N_L$  and from 0.165 to 0.248 for  $\rho$ . In all cases, the boundary ratio remains near 1 and the average number of nearest neighbors is approximately 4.8. In short, although the forms are constrained, there is no evidence to suggest that the basic diffusion process at work is distorted by changing the space in which the process operates.

In Figure 8.9, we show the 'signatures' for each of the eight structures, and it is quite clear that as the angle of arc  $\theta$  decreases, the fractal dimension  $D$  falls. In fact, in the vicinity of the central seed site, over-estimation of the dimension for the more complete systems changes to under-estimation as the wedge within which the system is contained decreases in angle. The dimensions based on  $D(\bar{R}_m)$ ,  $D(R)$  and the averages over  $D(R)$  are given in Table 8.7 where it is clear that  $D$  falls towards unity as the system is constrained. These changes in  $D$  have not been plotted here, but will be later in Figure 8.11. However, Table 8.7 suggests that we might easily find a

**Table 8.6.** Characteristics of the physically constrained baseline simulations

System characteristic	System shape based on degrees of Arc							
	$2\pi$	$1.75\pi$	$1.5\pi$	$1.25\pi$	$\pi$	$0.75\pi$	$0.5\pi$	$0.25\pi$
Lattice dimension	All lattices based on the original $150 \times 150$ grid							
Lattice points, $N_L$	22,500	19,687	16,875	14,062	11,250	8437	5625	2812
Occupied points, $N$	1856	1433	1108	792	672	639	451	251
$N/N_L$	0.082	0.073	0.066	0.057	0.059	0.076	0.080	0.089
Lattice radius, $R_{max}$	All $R_{max} = 75$							
Cluster radius, $R_m$	49.366	50.000	50.804	49.396	50.448	50.290	51.400	51.088
$R_m/R_{max}$	0.658	0.660	0.677	0.659	0.673	0.670	0.685	0.681
Mean distance, $\bar{R}$	27.183	24.635	22.559	19.609	22.617	25.331	31.662	33.526
$\bar{R}/R_m$	0.544	0.493	0.444	0.397	0.448	0.504	0.616	0.656
Average density, $\rho$	0.236	0.208	0.183	0.165	0.168	0.213	0.216	0.248
Boundary ratio, $\vartheta$	0.959	0.959	0.960	0.965	0.979	0.972	0.969	0.952
Nearest neighbors, $\xi$	4.862	4.868	4.839	4.828	4.812	4.789	4.896	4.741

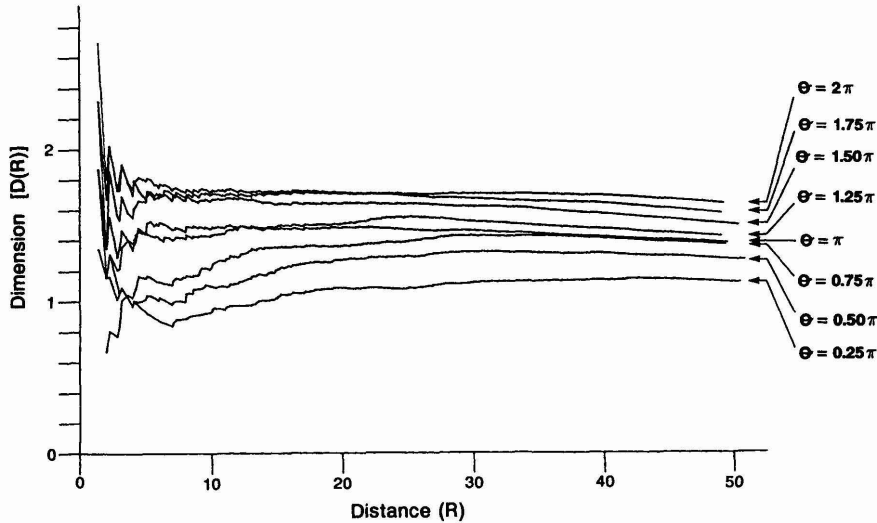


**Figure 8.9.** Fractal signatures of the sectorally constrained simulations.

**Table 8.7.** Fractal dimensions associated with the physically constrained baseline simulations

Angular variation $\theta$	$D(R_m)$	$D(\bar{R})$	Average over all $D(R)$
$2.00\pi$ ( $360^\circ$ )	1.556	1.708	1.681
$1.75\pi$ ( $315^\circ$ )	1.516	1.707	1.647
$0.50\pi$ ( $270^\circ$ )	1.479	1.677	1.628
$1.25\pi$ ( $225^\circ$ )	1.508	1.637	1.591
$1.00\pi$ ( $180^\circ$ )	1.387	1.499	1.483
$0.75\pi$ ( $135^\circ$ )	1.417	1.413	1.355
$0.50\pi$ ( $90^\circ$ )	1.234	1.249	1.164
$0.25\pi$ ( $45^\circ$ )	1.093	0.945	0.974

well-fitting function relating  $D$  to  $\theta$ . This is as we expected, but it also reveals that fractal dimension depends not only upon process but upon the geometry of the space within which the process takes place. Thus in explaining real urban form we must attempt to separate out the effects of both system geometry and the diffusion process control parameter  $\eta$  on spatial structure.

## 8.7 Generating the Continuum of Urban Forms

We are at last in a position to explore how different urban forms can be generated by varying the control parameter  $\eta$ . The effect of  $\eta$  on form has

already been explained, but we will summarize it briefly for convenience. In equation (8.8) which determines the probabilities of sites being selected for growth on the boundary of the cluster, as  $\eta$  increases, sites with the greatest probability of selection become dominant. As  $\eta \rightarrow 0$ , sites become more equiprobable for selection, whereas the baseline case where  $\eta = 1$ , implies a measure of normal control. As  $\eta \rightarrow \infty$ , the form generated becomes linear because the branch tips become highly probable for selection, whereas as  $\eta \rightarrow 0$ , a more amorphous, compact form emerges. As  $\eta \rightarrow \infty$ ,  $D \rightarrow 1$ , and as  $\eta \rightarrow 0$ ,  $D \rightarrow 2$ . If  $\eta$  is treated as a planning control, where control becomes total, it is possible to develop highly geometric city forms similar to the linear and grid cities of the urban idealists such as Le Corbusier and Frank Lloyd Wright which we introduced in the Chapter 1. When control is relaxed and  $\eta = 1$ , the city grows as a fractal structure, whereas when  $\eta \rightarrow 0$ , it could be argued that this too is a measure of control in which all sites are treated equally by the control agency.

We will generate nine urban forms, again including our coarse resolution simulation as the baseline. We will set  $\eta$  at 0, 0.25, 0.50, 0.75, at the baseline of  $\eta = 1$ , and at 2, 3, 4 and 5. The constraint on growth is as previously specified in that, once the cluster reaches  $0.66R_{max}$  ( $\approx 50$ ) units of distance from the central seed site, growth will terminate. This means that there are many more particles contained in structures with low values of  $\eta$ . The nine forms generated are shown in Plates 8.3 and 8.4. There is little need for comment as the forms bear out all the prior speculation which we made earlier. The range is from linear to concentric with the dendritic fractal structures forming the middle of the continuum. In Table 8.8, we show the physical characteristics of these nine forms, and we also note the computer time used to simulate each. The number of particles varies quite widely from  $N = 4735$  when  $\eta = 0$  to  $N = 121$  when  $\eta = 5$ . This is reflected in the CPU times reported which range from between five and seven hours when  $\eta < 1$  to only 22 minutes for  $\eta = 5$ . As we have shown previously, the densities depend upon the number of particles allocated and these range widely from  $\rho = 0.627$  to  $\rho = 0.016$ , thus illustrating how  $\eta$  affects the compactness of the resulting cluster. The percentage of particles on the bound-

**Table 8.8.** Characteristics of the continuum of urban forms

System characteristic	Urban form based on the control parameter $\eta$								
	$\eta = 0$	$\eta = 0.25$	$\eta = 0.50$	$\eta = 0.75$	$\eta = 1$	$\eta = 2$	$\eta = 3$	$\eta = 4$	$\eta = 5$
CPU time (h:min)	6:45	7:17	6:14	5:41	5:02	1:04	0:40	0:23	0:22
Lattice points, $N_l$	All $N_l = 22,500$								
Occupied points, $N$	4735	3792	2639	2154	1856	404	252	132	121
$N/N_l$	0.210	0.169	0.117	0.096	0.082	0.018	0.011	0.006	0.005
Lattice radius, $R_{max}$	All $R_{max} = 75$								
Cluster radius, $R_m$	49.041	50.010	51.478	49.366	49.336	49.031	49.010	49.092	49.366
$R_m/R_{max}$	0.654	0.667	0.686	0.658	0.667	0.654	0.653	0.654	0.658
Mean distance, $\bar{R}$	27.436	26.239	24.844	25.773	27.183	19.332	22.439	18.433	20.323
$\bar{R}/R_m$	0.559	0.525	0.483	0.522	0.544	0.394	0.458	0.376	0.412
Average density, $\rho$	0.627	0.483	0.317	0.281	0.236	0.053	0.033	0.017	0.016
Boundary ratio, $\vartheta$	0.552	0.719	0.878	0.926	0.959	1.000	1.000	1.000	1.000
Nearest neighbors, $\xi$	7.103	6.488	5.729	5.255	4.862	3.832	3.444	3.152	2.909

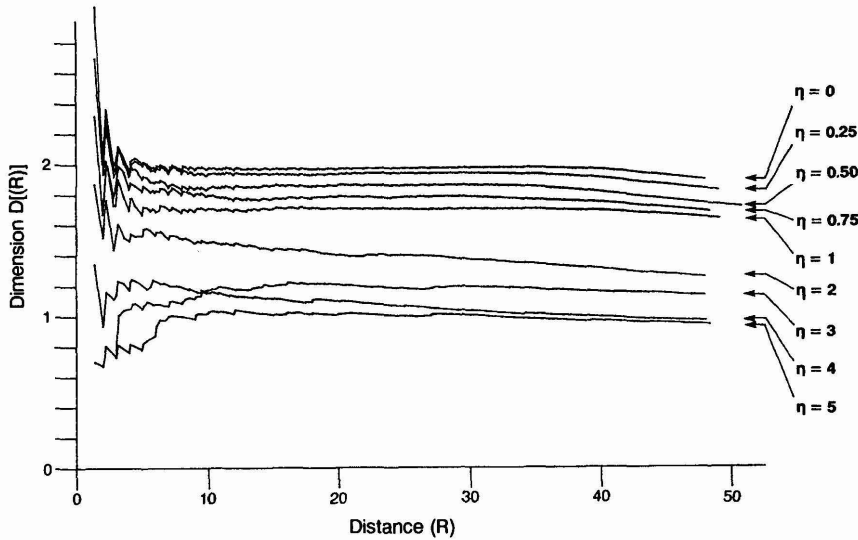


**Figure 8.10.** Fractal signatures of the distorted field simulations.

ary of the cluster is also affected by the type of form generated with an increasing number of interior points as the structure becomes more compact and  $\eta \rightarrow 0$ . The average number of nearest neighbors is a good measure of compactness and this ranges from 7.103 when  $\eta = 0$  to 2.909 when  $\eta = 5$ . All these measures reflect the change in density and the increasing size of the cluster as  $\eta \rightarrow 0$ .

The next and most crucial stage of our investigation is to estimate the fractal dimensions of these nine clusters. Using equation (8.13), we have plotted the signatures for each of these forms in Figure 8.10. As expected, the average fractal dimensions fall as  $\eta \rightarrow \infty$  and in Table 8.9, these values are shown for each cluster based on the use of equation (8.13) for  $R_m$ ,  $\bar{R}$  and the average of  $D(\bar{R})$  over the profiles shown in Figure 8.10. As in the case of the fractal dimensions computed for different angular spatial systems and shown earlier in Table 8.7, it is easy to find a function which

**Table 8.9.** Fractal dimensions associated with the continuum of urban forms

Control parameter $\eta$	$D(R_m)$	$D(\bar{R})$	Average over all $D(R)$
0	1.879	1.971	1.964
0.25	1.814	1.938	1.924
0.50	1.708	1.858	1.847
0.75	1.675	1.782	1.769
1.00	1.631	1.701	1.698
2.00	1.248	1.409	1.417
3.00	1.127	1.187	1.185
4.00	0.960	1.110	1.060
5.00	0.776	1.009	0.976

predicts  $D$  from  $\eta$ . In Figure 8.11, we have plotted these dimensions from  $D(\bar{R})$  in Table 8.9 against  $\eta$ , and from Table 8.7 against  $\theta$ . One obvious problem in any real structure for which its fractal dimension can be computed, is to isolate the effects of control  $\eta$  from spatial constraint, measured here by  $\theta$ . This will preoccupy us in the next section when we apply these ideas to the medium-sized town of Cardiff. We have also applied one-point and two-point estimation procedures to these nine forms and, although the estimated dimensions follow the same graphs as those shown in Figure 8.11, the results are poor, the procedures somewhat volatile; it thus of little worth to report them here.

## 8.8 Measuring and Simulating Urban Form in Medium-Sized Towns: Applications to Cardiff

We have now developed enough insight into the continuum model to make comparisons with real urban growth and to consider how the processes of growth embedded in the model might enable simulation of real forms. In the last chapter, we simply contrasted the DLA model and the form generated with the form of the medium-sized English town of Taunton. Several of the measurements of both the theoretical and actual forms were similar,

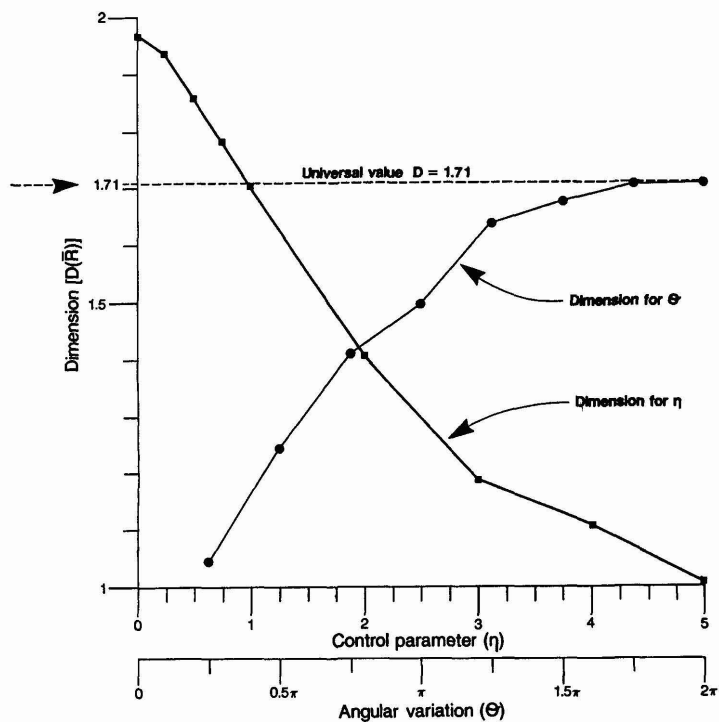


**Figure 8.11.** Relationships between the fractal dimension, spatial constraint parameter  $\theta$ , and the planning control parameter  $\eta$ .

but their fractal dimensions were not. We now have a much more robust method of estimation, we have a parameter which enables us to control the compactness, hence fractal dimension of the resultant forms, and we have some insight into the way geometry and physical constraints on the growth space affect dimension. Thus it should be possible to begin some simulations of a real urban system. As a first stage in this quest, we will measure the physical characteristics of Cardiff, and estimate its fractal dimension.

Cardiff was digitized from the 1:50,000 scale map, the area being divided into 50 m grid squares which yielded a  $150 \times 150$  lattice, making comparison with our theoretical structures possible. The extent of urban growth is shown in Figure 8.12 where it is clear that the center of the urban area which is the original Roman site and the site of the medieval castle, is not at the center of the lattice. In terms of the  $150 \times 150$  grid, this location is at  $(x = 81, y = 66)$ . Moreover, the digitized urban area which comprises all land uses except open space, covers the entire extent of the lattice because there are many villages and disconnected clusters of urban development around the town. The maximum lattice radius  $R_{\max}$  is not meaningful for a cluster which is off-center on the lattice, and because of the extent of urban development, the maximum cluster radius from the center is  $R_m \approx 110$  units of distance. This is twice the size of the clusters used in the simulations, and must be taken into account when comparisons are made below. Of the 22,500 lattice points, only 18,245 constitute the area for measurement and simulation: of the remaining points, 3849 are in the sea and 406 are inland waterways (rivers, canals and lakes).

The physical characteristics of Cardiff with respect to size and density

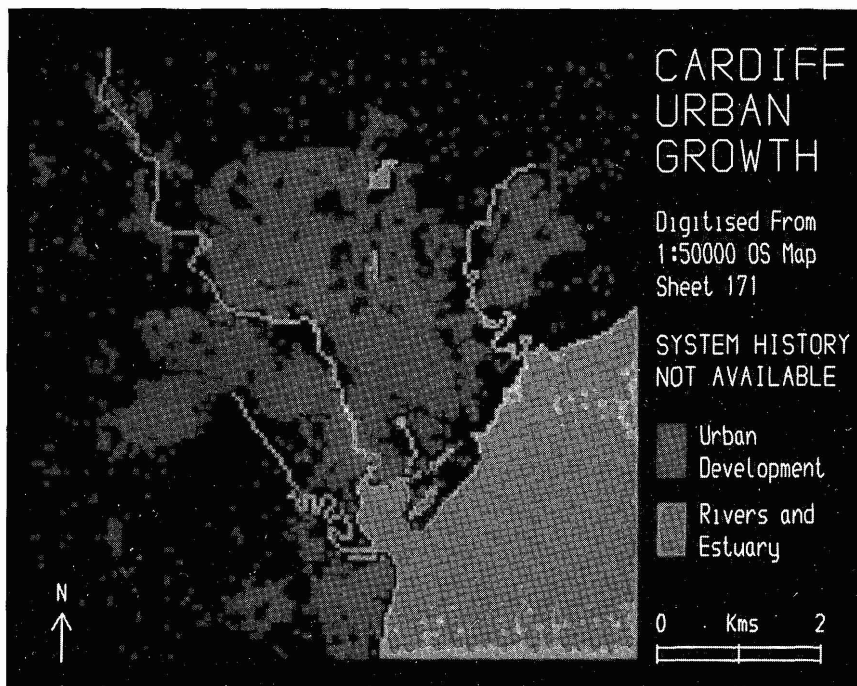


**Figure 8.12.** The urban development of Cardiff.

are shown in Table 8.10. As  $R_{\max}$  is not relevant, related statistics have not been computed. It is worth saying that we have explored ways in which the lattice can be extended to make the form symmetric so that some of the previous measures can be computed. This involves 'guessing' the composition of areas outside the map area in Figure 8.12, and although some useful techniques have been developed, these will not be reported here. From the measures for Cardiff in Table 8.10 and from the visual appreciation of urban form shown in Figure 8.12 and Plate 8.5, we need to speculate on the type of structure Cardiff displays with respect to the theoretical forms discussed previously. In Table 8.10, we have included three of the forms presented earlier in that these forms seem 'close' to Cardiff in some way. We have also included the coarse resolution  $\eta = 1$  model, which acts as the baseline. Examination of the shape of Cardiff in Figure 8.12 indicates that the urban form is similar to that shown in Plate 8.2 based on the angular sector  $\theta = 1.25\pi$  simulation. However, with respect to the percentage of lattice cells excluded, the simulation based on  $\theta = 1.75\pi$  is closer, and thus this has also been included in Table 8.10. We will comment on the inclusion of the  $\eta = 0.75$  model in this table below, but note also that the average number of nearest neighbors in Cardiff and the boundary ratio suggest a form based on  $\eta = 0.50$ . Last, it is clear that Cardiff has much more development than most of the theoretical simulations here, and this indicates that in future work, some thought should be given to growing larger theoretical clusters or excluding development clearly not part of the main cluster under analysis in real applications.

To proceed with this comparison, the 'signature' of the Cardiff cluster must be examined, and this is illustrated in Figure 8.13. In comparing this with earlier figures, it has some similarities – short-range volatility of dimension in the vicinity of the origin and a long-range edge effect but in the inner area around the seed point, the dimension drops sharply, quickly recovering to a stable value over most of its profile. At the edge of the

**Table 8.10.** Characteristics of Cardiff and relevant urban forms

System characteristic	Cardiff	Closest comparators			
		1.25 $\pi$	1.75 $\pi$	$\eta=0.75$	$\eta=1$
Lattice dimension	All lattices based on the original 150 $\times$ 150 grid				
Lattice points, $N_l$	18,245	16,875	19,687	22,500	22,500
Occupied points, $N$	5067	1108	1433	2154	1856
$N/N_l$	0.278	0.066	0.073	0.096	0.082
Lattice radius, $R_{\max}$	—	75	75	75	75
Cluster radius, $R_m$	110.318	50.804	50.000	49.366	49.366
$R_m/R_{\max}$	—	0.677	0.666	0.658	0.667
Mean distance, $\bar{R}$	41.539	22.559	24.635	25.773	27.183
$\bar{R}/R_m$	0.377	0.444	0.493	0.522	0.544
Average density, $\rho$	0.164	0.183	0.208	0.281	0.236
Boundary ratio, $\vartheta$	0.612	0.960	0.959	0.926	0.959
Nearest neighbors, $\xi$	5.833	4.839	4.868	5.255	4.862

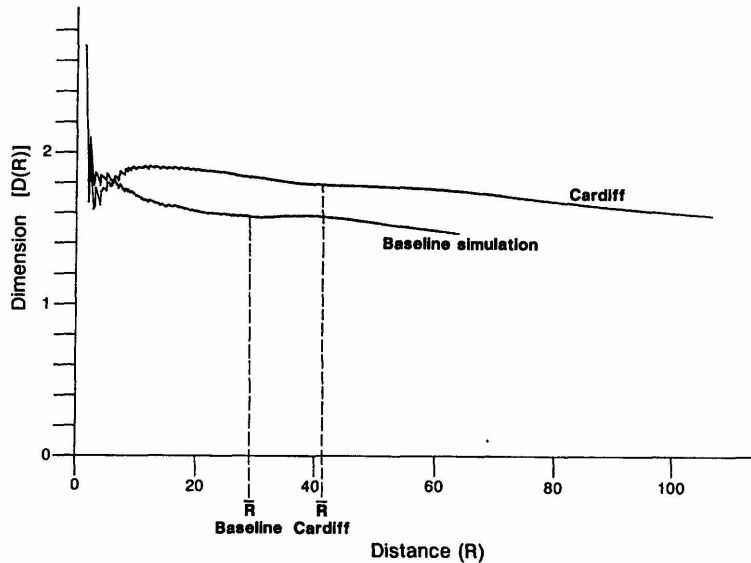


**Figure 8.13.** Fractal signatures of Cardiff and the baseline simulations in Cardiff's urban field.

cluster,  $D(R_m) = 1.570$  whereas at the mean,  $D(\bar{R}) = 1.786$ . The average over all dimensions shown in Figure 8.13 is 1.772 and thus it is clear that the fractal dimension of Cardiff is higher than the fractal  $\eta = 1$  case, thus suggesting that  $\eta < 1$ . From the earlier analysis, a fractal dimension in the order of 1.78 suggests that the control parameter  $\eta$  is more likely to be 0.75 than 1, hence the inclusion of this in Table 8.10.

However, examining the level of physical constraint in Table 8.7 seems to suggest that the fractal dimension associated with the physical characteristics of Cardiff would be around 1.60. To generate such a form through simulation would probably require  $\eta$  to be set much lower, perhaps at 0.5 or even below this, implying a much more even potential field than the  $\eta = 1$  fractal case is able to generate. This will be explored below in the simulations, but first it is worth making one last point on estimation. We have also computed the one-point and two-point measures for Cardiff and used these to estimate fractal dimensions using regression. The results are disappointing as in other cases tested in this chapter. However, what is more worrying is that the dimensions produced are lower than the universal value of  $D = 1.7$ . For the one-point measures,  $D$  varies from 1.29 to 1.49. This also brings into doubt the results in the previous chapter where the fractal dimensions of Taunton were also lower than 1.7. However, the purpose of this research is not to aim for consensus with respect to dimension, but to derive better methods of estimation and simulation. The estimation procedure introduced in equation (8.13) clearly enables such progress to be made.

The ultimate focus of this research is on the design of a physical simulation model built on simple and thus intuitively attractive processes which govern urban growth. To this end, it is worth summarizing the assumptions of the continuum model. First, there is diffusion from a source of low to

high potential, but constrained so that the resulting cluster remains intact or connected. In short, higher potential exists in areas away from the source where there is more space for expansion, but the cluster must remain intact as it realizes this higher potential through growth. Second, physical constraints which reduce space must act as barriers to development, but must not reduce potential *per se*. Third, the resultant form based on the best realization of space potential can be distorted by a control parameter which modifies the relative distribution of potential for growth on the boundary of the cluster. Last, the number of seed sites which initiate growth should be kept to a minimum, ideally to one site.

The first simulation attempted simply uses the fractal ( $\eta = 1$ ) baseline model with its seed site at  $(x = 81, y = 66)$  on the  $150 \times 150$  lattice, with the physical constraints of rivers and sea acting as limits on the area of the lattice in which it is legitimate for growth to take place. The resulting form is shown in Figure 8.14 from which several points immediately emerge. Cardiff does not grow towards its port which is some two miles from the medieval center and on the coast. This port only opened up in the mid-19th century as the South Wales coalfield developed (Daunton, 1977), and this would suggest that another 'seed' site is required. The town also grows in the area between the River Taff (the longest, middle river in Figure 8.12) and the eastern River Rhymney. Because of these physical constraints, growth is unable to spread across these barriers and thus the need for bridging is identified. Last, the cluster grown in Figure 8.14 consists of only 808, not 5067 particles, and this reinforces the requirement that more areas be opened up to growth.

Four more simulations have been attempted in which a second seed site

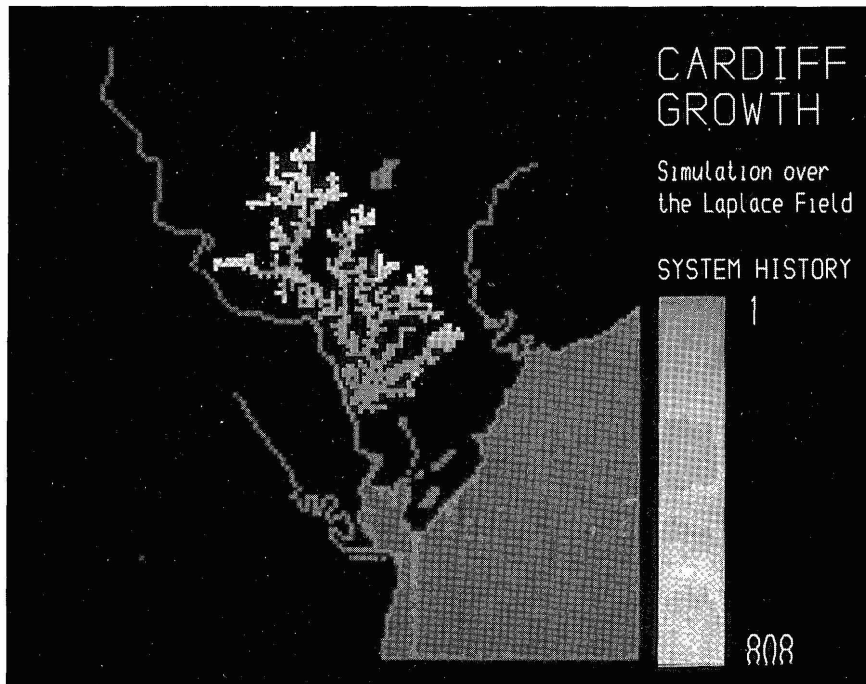


**Figure 8.14.** The baseline simulation in Cardiff's urban field.

is planted in the Cardiff docklands after 80 particles have been generated. Two bridges (breaks in the river constraint) have been established across the River Taff west of the medieval center and docklands, and one bridge has been made across the River Rhymney in the east. It would be easily possible to build in decision rules to generate bridges at suitable points if the pressures of growth became substantial, but in the interests of parsimony, these changes have been kept to a minimum. Simulations of the continuum model on the Cardiff lattice have been run with  $\eta = 1, 0.75, 0.50$  and  $0.25$ , and the resultant urban forms are shown in Plate 8.6. It is clear now that growth spans the rivers, and on the west bank of the Taff, development occurs later than in sites at a similar distance north of the center. But it is only when  $\eta < 0.5$  that sufficient growth is generated, and the docklands begin to exert a major effect upon development.

If we examine the fractal dimensions of these four simulations, we find that the physical constraints exert a powerful effect. For the case of the single-seed-site simulation shown in Figure 8.14, we have plotted its signature earlier alongside that of Cardiff in Figure 8.13. For this simulation,  $D(\bar{R}) = 1.460$ . In Figure 8.15, the signature profiles are shown for the four simulations based on  $\eta = 1, \eta = 0.75, \eta = 0.50$  and  $\eta = 0.25$  which incorporate the two seed sites and bridging developments. These generate fractal dimensions of  $D(\bar{R}) = 1.574, 1.595, 1.704$  and  $1.820$  respectively in comparison to their non-constrained equivalents  $D(\bar{R}) = 1.701, 1.782, 1.858$  and  $1.938$  given earlier in Table 8.9. On this basis, we might speculate that a model with  $\eta$  about  $0.35$  might provide the best simulation for Cardiff. This implies a degree of control which might be exercised by many single landowners in competition or, perhaps, large landowners in collusion.

These simulations are designed to be suggestive, not definitive. They indicate how we might proceed. When these models are demonstrated, they tend to evoke considerable reaction, especially when it is realized that

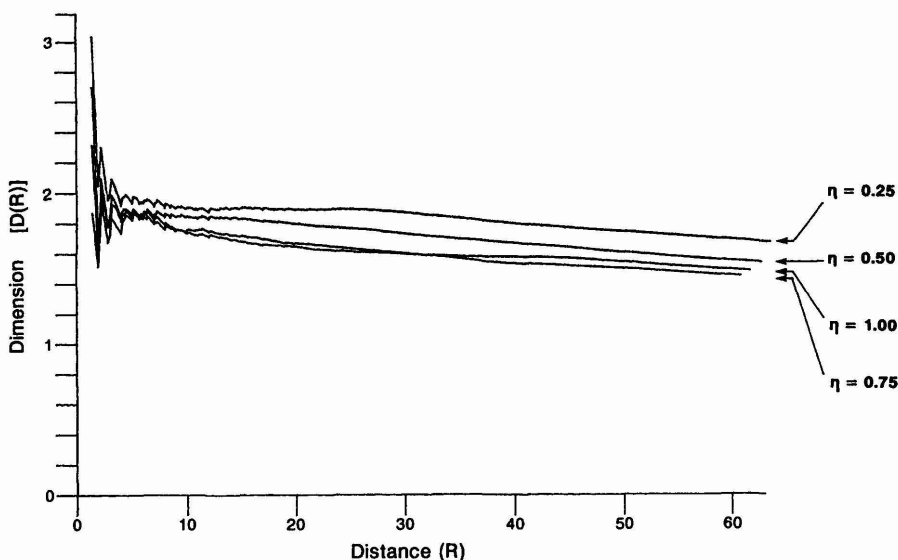


**Figure 8.15.** Fractal signatures of the Cardiff simulations.

physical constraints guide the simulation. Colleagues are quick to point out many obvious extensions which might make the growth processes more realistic. But the value of the model as it stands is in its *parsimony*. Rather than introduce more decision rules into the structure, there is an urgent need to examine the role of seed sites, and explore the dynamics of the model further. For this, we need better data on the historical evolution of the city, and if we had this, the importance of seed sites could be better assessed. We would then be in a position to examine thoroughly the role of physical constraints on urban growth, and to progress the model towards more realistic simulations. As it stands, our simulations indicate the importance of DLA and DBM to the generation of entire classes of city, but as yet, such simulations are far from the point where they might be used to make explicit forecasts.

## 8.9 Towards More Realistic Models

The continuum model based on DBM which uses Laplace's equation, its consequent solution, and the way the potential field can be controlled or distorted, clearly produces a model which is much easier to explore than the random walk version of DLA. Indeed, this specification of the model is an essential step in the process of moving towards simulation of real urban systems as has been demonstrated here for Cardiff. There are, however, several urgent developments to initiate. It is necessary to treat much larger lattices and readers with supercomputer resources such as Connection Machines whose architecture is adapted to Laplace field problems, must be encouraged to explore  $1000 \times 1000$  lattices or even larger ones for this type of problem (Dewar and Harris, 1986). It is also necessary to think about three-dimensional lattices and DLA simulation, which might capture some of the characteristics of urban systems, but, wherever this research seems to offer promising insights, the issue of computer resources and time is paramount. More realistic DBM models are also possible, and it would be useful to adapt many of these to the simulation of city systems (Wiesmann, 1989).

We need to extend our research into the interaction between physical constraints on space and the control of the potential field and probabilities of occupancy around cluster boundaries. We have not rigorously examined the types of forms generated for different combinations of  $\theta$  and  $\eta$ , although the inferences made here on the basis of our partial explorations are unlikely to be badly wrong. We also require a better investigation of physical indices, and it would be useful if we could classify different urban forms with respect to a variety of such indices as well as the spatial ( $\theta$ ) and planning control ( $\eta$ ) parameters. Many of these developments are already taking place in the burgeoning field of cluster growth modeling within mathematical physics, and there is much to learn from current and future developments in those domains. But by adapting cluster models more closely to the characteristics of urban development such as discontinuous form, reversible aggregation and the possible interaction of different cluster processes, that

is interlocking and interacting DLA processes operating with different types of development but in the same system, considerable progress can be made with the approach we have begun to outline here.

Finally, we need better measurements of urban development and density. In the last chapter, we were concerned that our measurement of real form was at too coarse a level to pick up the appropriate pattern of urban structure. The same difficulties apply here, and there is no substitute for finer resolution to our detection of development patterns. All this demonstrates is that once again, in the search for universals, whether it be in qualitative matters or in the social physics which we are espousing here, it is necessary to proceed with rigor on all fronts. In this chapter, we have clearly demonstrated that the same fractal dimensions can be generated through different combinations of physical constraint and planning control. This in turn brings into question the role of a fixed scale from which all measurements are taken and simulations initiated. To make further progress, it is necessary to explore the interaction of physical constraints at different scales more rigorously, and to this end, many more real urban applications are required.

In the next chapter, we will change tack once again, but in the quest to extend the ideas of this and the last chapter to more mainstream urban theory and analysis. We have almost unwittingly begun to home in upon the idea of urban density, and as a first step in showing how our theory of the fractal city might inform the mainstream, we will explore how existing approaches to urban density analysis can be enriched and reformulated in Chapter 9. This will involve us in theories of urban allometry, and these we will take further in Chapter 10 when we will move full circle to show how fractal geometry can begin to inform questions of city size and distribution, so long the traditional preserve of human geography through central place theory.